Precision Magnetic Suspension Linear Bearing

David L. Trumper, Michael A. Queen
Dept. of Electrical Engineering
Univ. of N. Carolina at Charlotte
Charlotte, NC 28223

1 Introduction

Magnetic bearings represent a promising approach for achieving positioning with nanometer resolution. The first author has constructed a high-precision linear bearing which demonstrates 5 nm short-term position stability. This system represents the experimental implementation of an idea presented in [1] and has been investigated as part of the first author's Ph.D. thesis [2].

This study was initiated with support from the Molecular Measuring Machine (M^3) project at the National Institute of Standards and Technology [3]. The form-factor of the bearing was thus chosen such that it was compatible with the M^3 crossed-slide design. The bearing technology is also highly suitable for other precision applications, such as in stages for photolithography and diamond turning machines; these application areas provide the focus for our current research.

As shown in Figures 1–4, a 10.7 kg platen measuring 125 mm by 125 mm by 350 mm is suspended and controlled in five degrees of freedom by seven electromagnets, labelled as $B1$ through $B7$. Five capacitive probes located in the bearing centers measure position with nanometer resolution. The seven points at which the bearing forces act on the platen are shown as arrows and the five points at which the position measurements are taken are indicated as dots in Figure 1. The scale of Figures 2, 3, and 4 is indicated by the 100 mm reference shown in Figure 2.

The suspension acts as a linear bearing, allowing linear travel of 50 mm in the long axis of the platen. In previous work [2,4], the long-travel degree of freedom is not actively controlled. Efforts are currently directed at achieving control of this degree of freedom with 50 mm travel through a novel magnetic suspension linear motor. This motor consists of an array of permanent magnets attached to the moving platen and a stator array of coils attached to the fixed machine frame as shown in Figs. 2–4. Prototypes of this linear motor are currently under construction. Position in this degree of freedom is transduced by a laser interferometer. For simplicity, optics for this interferometer are not shown in the figures.

The key feature of the linear motor is that it affords control of forces in two degrees of freedom, one parallel to the air gap and lying on the axis of the magnet array and one perpendicular to the air gap. Thus it is possible to simultaneously control translation and suspension with a single motor structure. The motor design and control are the focus of this

C-2

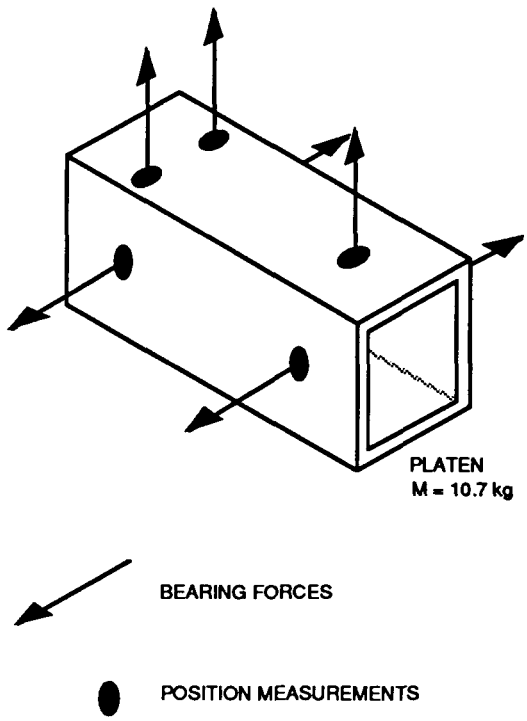

Figure 1: Points at which bearing forces are applied to platen, and points at which platen position is measured.

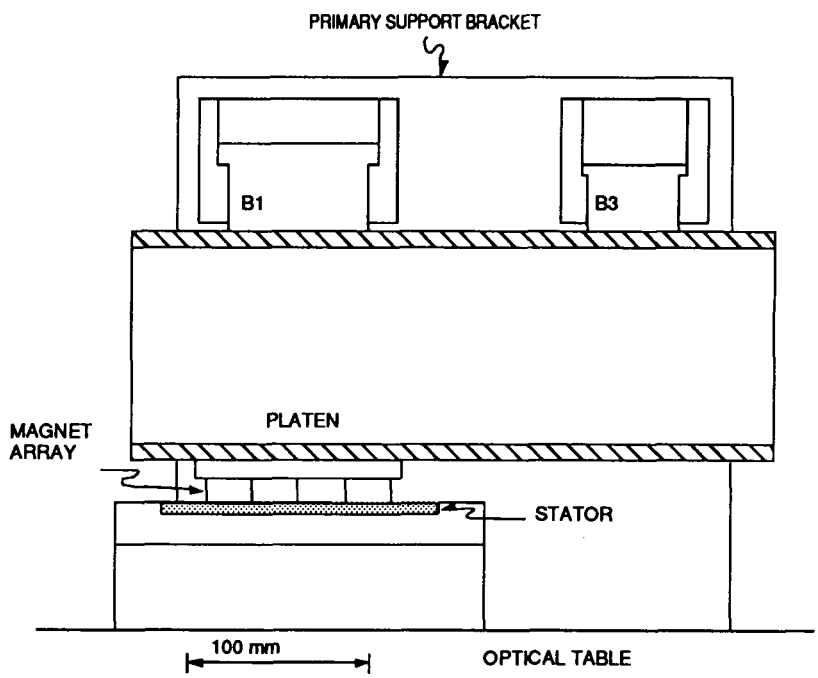

Figure 2: Side view of bearing and linear motor assembly.

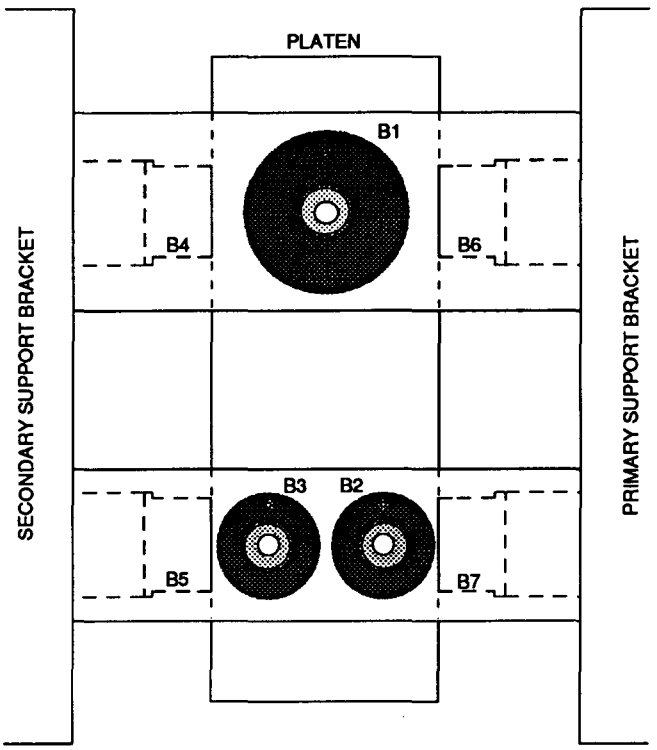

Figure 3: Top view of bearing and linear motor assembly.

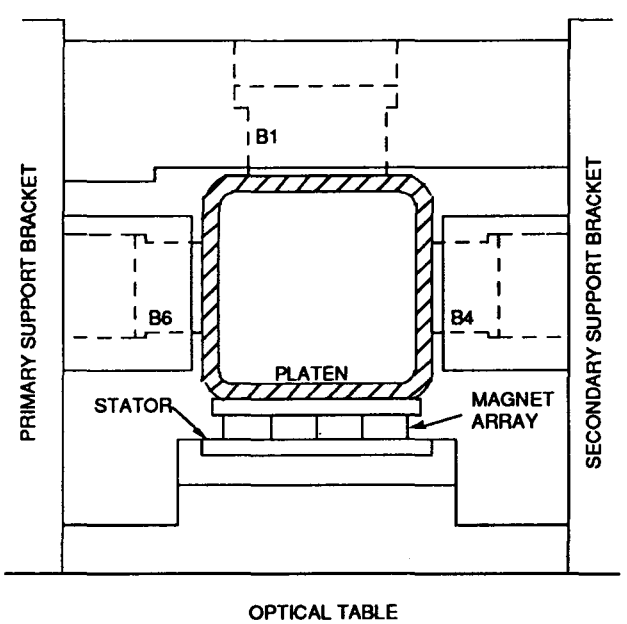

Figure 4: End view of bearing and linear motor assembly.

paper.

The paper is organized as follows. In the next section, the electromechanical characteristics of the linear motor are developed, and an example design is presented. With these results in hand, it is then shown how two degrees of freedom can be controlled using this linear motor. Following this, the conceptual design for a precision X-Y stage driven by four such motors is described. It is anticipated that this stage can achieve nanometer motion control, with travel in X and Y of several hundred millimeters. Finally, suggestions for further work are presented.

2 Motor fields and forces

To calculate the electromagnetic forces, the motor is idealized as a two dimensional structure as shown in Figure 5. Here, the motor is assumed to have a depth of w into the paper and to extend indefinitely in the $\pm z$-direction. The stator is fixed in the laboratory frame x, y, z. The primed coordinate frame x', y', z' is fixed in the layer of magnetization, and is displaced from the unprimed frame by $(x_0 + \Delta)\overline{i_x} + z_0\overline{i_z}$.

The magnet array is modeled by a half-infinite region of sinusoidally distributed, x-directed magnetization $M_x = \mathrm{Re}M_0 e^{-jkz'}$. The magnetization layer is referred back to the unprimed frame by substituting $z' = z - z_0$ into M_x which gives $M_x = \mathrm{Re}\tilde{M}e^{-jkz}$, with complex amplitude $\tilde{M} = M_0 e^{jkz_0}$.

The stator is modeled by a sinusoidally distributed, y-directed current density $J_y = \mathrm{Re}\tilde{J}e^{-jkz}$, in a layer from $x = 0$ to $x = \Delta$. The complex amplitude $\tilde{J}$ is a function of the winding density η_0, and the two phase currents, I_1 and I_2. Specifically, $\mathrm{Re}\tilde{J} = I_1\eta_0$ and $\mathrm{Im}\tilde{J} = I_2\eta_0$. Throughout this discussion, the complex amplitudes indicated by a tilde represent the temporal variations in both amplitude and spatial phase.

The model is idealized in several ways. First, while the stator current in the real motor is distributed down the axis of the motor in a spatial square-wave, in the model the current density is sinusoidally distributed at the spatial fundamental of the actual stator current distribution. Further, although the real magnets are of finite thickness and distributed in a spatial square-wave of magnetization, we model the magnetized region as of half-infinite extent and with the magnetization distributed sinusoidally in space at the spatial fundamental of the actual magnetization distribution. It is reasonable to model only the fundamental components of magnetization and current, as these are responsible for the bulk of the motor force production. The additional harmonics present in the actual motor can readily be added as Fourier series components built upon the solution we develop herein.

The fields and forces for the finite-thickness stator in Figure 5 are obtained by first studying a simpler model as shown in Figure 6, in which the excitation consists of a current sheet (spatial impulse). Then, with the finite-thickness stator current distribution written as an integral of spatially-distributed current sheets, the linearity of the solution is exploited to write the forces on the finite thickness stator in the form of a convolution integral. This integral is readily solved, yielding the forces on the finite thickness stator.

The analysis follows the techniques and notation from [5], chapters 2, 3, and 4. The

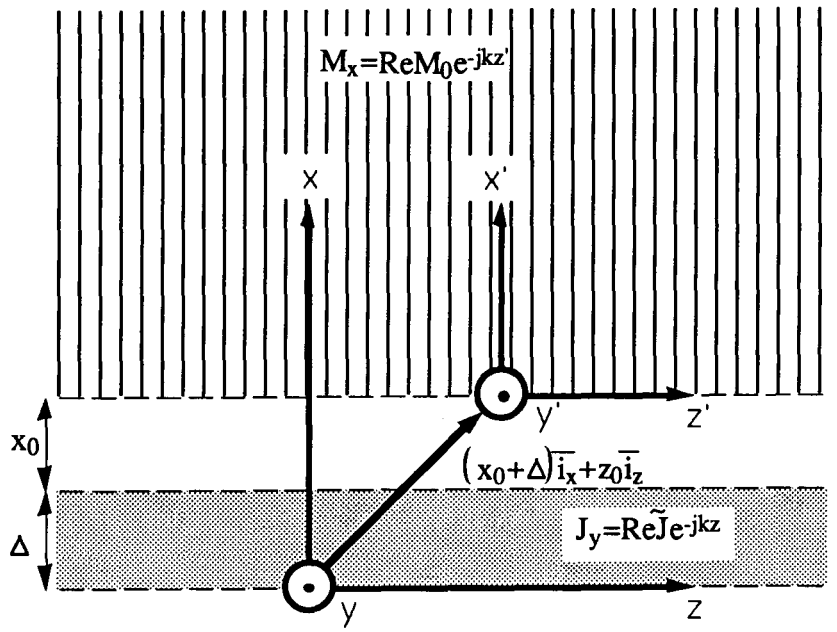

Figure 5: Geometry which represents the current density model of linear motor.

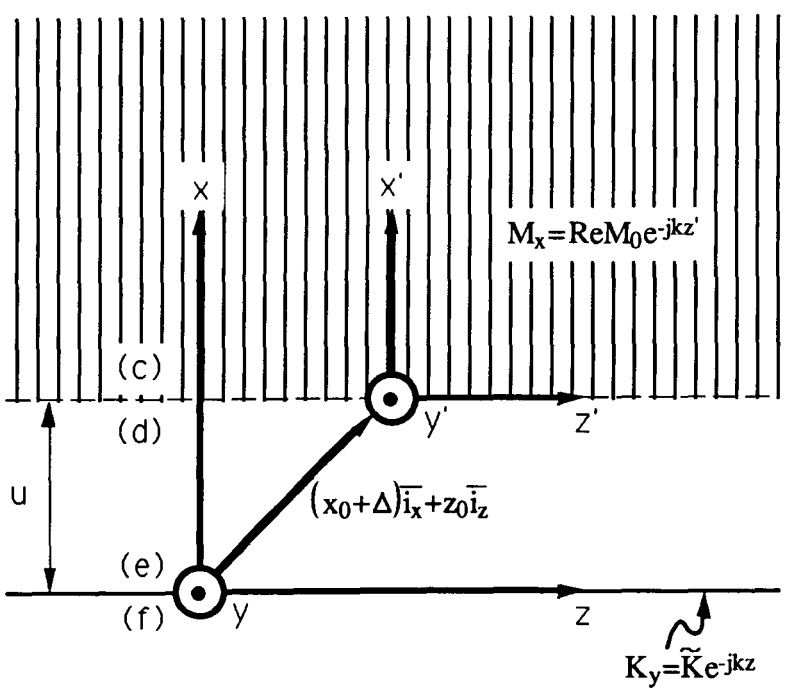

Figure 6: Geometry which represents current sheet model of linear motor.

magnetic field is given as the gradient of the magnetic scalar potential $\mathbf{H} = -\nabla\psi$. Fields and potentials are represented as the real part of a complex amplitude multiplied by a complex exponential in z. Superscripted letters denote a quantity evaluated at the corresponding boundary.

At the magnetization boundary the potential is continuous, $\tilde{\psi}^c = \tilde{\psi}^d$, and the normal field is discontinuous by the magnetization, $\tilde{H}_x^c - \tilde{H}_x^d = -\tilde{M}$. At the current sheet, normal H is continuous, $\tilde{H}_x^e = \tilde{H}_x^f$, and the tangential field is discontinuous by the value of the surface current, $\tilde{H}_z^e - \tilde{H}_z^f = -\tilde{K}$, or alternatively $\tilde{\psi}^e - \tilde{\psi}^f = j\frac{\tilde{K}}{k}$. These boundary conditions are summarized below

$$\tilde{\psi}^c = \tilde{\psi}^d \tag{1}$$

$$\tilde{H}_x^e = \tilde{H}_x^f \tag{2}$$

$$\tilde{\psi}^e - \tilde{\psi}^f = j\frac{\tilde{K}}{k} \tag{3}$$

$$\tilde{H}_x^c - \tilde{H}_x^d = -\tilde{M} \tag{4}$$

Applying the transfer relations from Section 2.16 of [5] yields the following four equations among the field and potential complex amplitudes at the boundaries.

$$\tilde{H}_x^c = k\,\tilde{\psi}^c \tag{5}$$

$$\tilde{H}_x^d = -k\coth(ku)\,\tilde{\psi}^d + \frac{k}{\sinh(ku)}\,\tilde{\psi}^e \tag{6}$$

$$\tilde{H}_x^e = \frac{-k}{\sinh(ku)}\,\tilde{\psi}^d + k\coth(ku)\,\tilde{\psi}^e \tag{7}$$

$$\tilde{H}_x^f = -k\,\tilde{\psi}^f \tag{8}$$

where $u = x_0 + \Delta$.

Together, equations (1)–(8) form a set of eight equations in eight unknowns, which are driven by the sources M_x and K_y.

In order to calculate the normal and tangential forces exerted on the platen, the potential and normal field at boundary (d) are calculated from equations (1)–(8) as:

$$\tilde{\psi}^d = \frac{1}{2k}(j\tilde{K}e^{-ku} - \tilde{M}) \tag{9}$$

and

$$\tilde{H}_x^d = \frac{1}{2}(j\tilde{K}e^{-ku} + \tilde{M}). \tag{10}$$

The tangential field $\tilde{H}_z^d$ is related to the potential $\tilde{\psi}^d$ by the negative of the gradient with respect to z. Thus

$$\tilde{H}_z^d = -\frac{1}{2}(\tilde{K}e^{-ku} + j\tilde{M}). \tag{11}$$

The force acting on a volume of the magnet array is given by the integral of the Maxwell stress tensor over the surface enclosing this volume. For a spatially-periodic structure, the

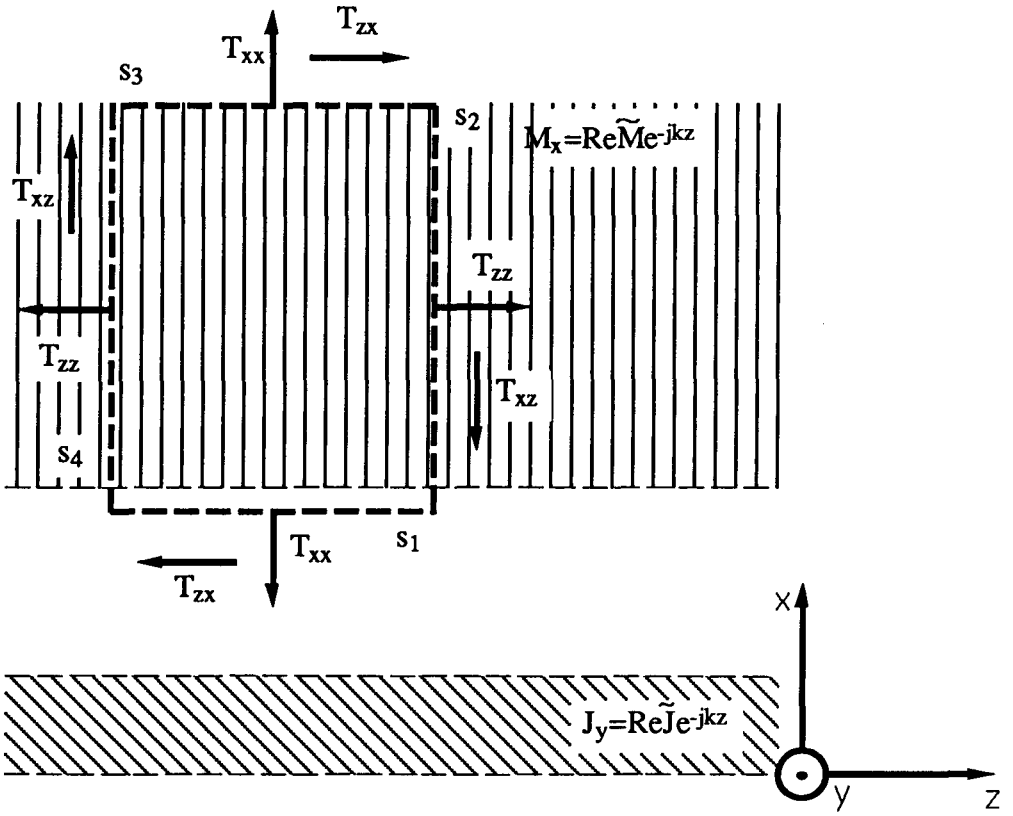

Figure 7: Showing the components of the Maxwell stress tensor acting on a surface which is used to find the forces acting on the magnet array.

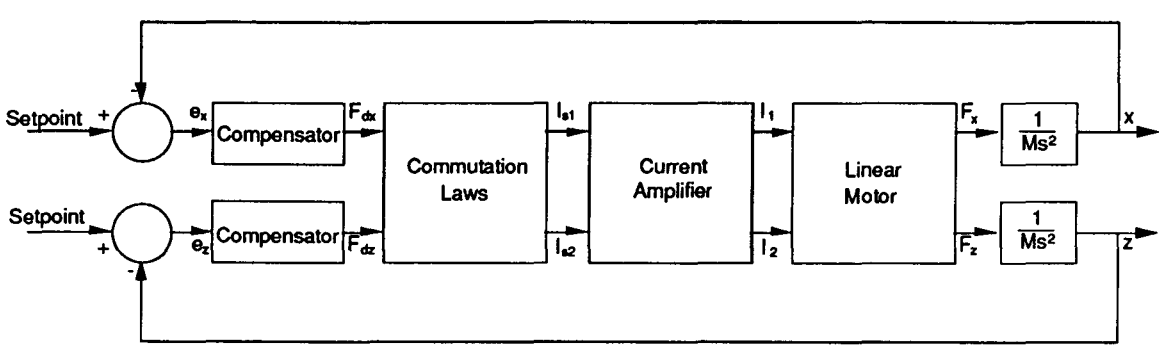

Figure 8: Two degree of freedom control loop block diagram.

integration is simplified if the volume encloses a single spatial period. The components of the stress tensor acting on such a volume are shown in Figure 7. The integrals of T_{xx} and T_{zx} on surface s_3 are found to equal zero. Also, the T_{xz} and T_{zz} components on s_2 and s_4 cancel, since these surfaces are one spatial wavelength apart. The only non-zero contribution is on s_1. Over an integer number of spatial periods, this force can be written as the spatial average on z multiplied by the area of the surface. Specifically, the normal force acting on one spatial period of the magnet array is given by

$$F_x = -A_m \langle T_{xx} \rangle_z \tag{12}$$

where the expression $\langle \cdot \rangle_z$ stands for the spatial average with respect to z and $A_m = w2\pi/k$ is the area of one spatial period of the motor. Similarly, the tangential force is given by

$$F_z = -A_m \langle T_{zx} \rangle_z . \tag{13}$$

The minus signs in these expressions are accounted for by the direction of the stress tensor components acting on s_1 which is the *bottom* surface.

The stress tensor for magnetically-linear materials derived from the Korteweg-Helmholtz force density ([5], section 3.10) is

$$T_{ij} = \mu H_i H_j - \frac{\mu}{2} \delta_{ij} H_k H_k \tag{14}$$

using the Einstein summation convention where since the k's appear twice in the same term they are to be summed from one to three. A final useful identity is the averaging theorem ([5], section 2.15).

$$\left\langle \mathrm{Re}\tilde{A}e^{-jkz} \mathrm{Re}\tilde{B}e^{-jkz} \right\rangle_z = \frac{1}{2} \mathrm{Re}\tilde{A}\tilde{B}^* . \tag{15}$$

Applying equations (12)–(15) with the results (10) and (11), the forces are found to be

$$F_x = \frac{A_m \mu_0}{4} e^{-ku} \left(\mathrm{Im}(\tilde{K}) \mathrm{Re}(\tilde{M}) - \mathrm{Re}(\tilde{K}) \mathrm{Im}(\tilde{M}) \right) \tag{16}$$

and

$$F_z = \frac{A_m \mu_0}{4} e^{-ku} \left(\mathrm{Re}(\tilde{K}) \mathrm{Re}(\tilde{M}) + \mathrm{Im}(\tilde{K}) \mathrm{Im}(\tilde{M}) \right) . \tag{17}$$

Thus we have derived the forces acting on the magnet array due to a sinusoidally distributed current sheet separated from the magnet array by a distance u.

Returning to the finite thickness of sinusoidally distributed current density shown in Figure 5 the forces acting on the magnet array in this case can be determined by summing the forces due to multiple current sheets of the form shown in Figure 6. That is, we integrate from $x = 0$ to $x = \Delta$ the force on the magnet array resulting from a current sheet at location x with intensity $\tilde{K} = \tilde{J}dx$. Specifically,

$$F_x = \frac{A_m \mu_0}{4} \int_0^{\Delta} \left(\mathrm{Im}(\tilde{J}) \mathrm{Re}(\tilde{M}) - \mathrm{Re}(\tilde{J}) \mathrm{Im}(\tilde{M}) \right) e^{-k(\Delta + x_0 - x)} dx \tag{18}$$

and

$$F_z = \frac{A_m \mu_0}{4} \int_0^{\Delta} \left(\mathrm{Re}(\tilde{J})\mathrm{Re}(\tilde{M}) + \mathrm{Im}(\tilde{J})\mathrm{Im}(\tilde{M}) \right) e^{-k(\Delta + x_0 - x)} dx. \tag{19}$$

In writing these integrals, the separation distance $\Delta + x_0 - x$ between the differential current element and the magnet array lower surface has been used to replace u in (16) and (17). Since within the stator J is independent of x, evaluating these integrals gives

$$F_x = \frac{A_m \mu_0}{4k} \left(\mathrm{Im}(\tilde{J})\mathrm{Re}(\tilde{M}) - \mathrm{Re}(\tilde{J})\mathrm{Im}(\tilde{M}) \right) e^{-kx_0}(1 - e^{-k\Delta}) \tag{20}$$

and

$$F_z = \frac{A_m \mu_0}{4k} \left(\mathrm{Re}(\tilde{J})\mathrm{Re}(\tilde{M}) + \mathrm{Im}(\tilde{J})\mathrm{Im}(\tilde{M}) \right) e^{-kx_0}(1 - e^{-k\Delta}). \tag{21}$$

As stated earlier, the current density J is driven by two phase currents $\mathrm{Re}\tilde{J} = I_1 \eta_0$ and $\mathrm{Im}\tilde{J} = I_2 \eta_0$. The forces in terms of these phase currents are found by using these relations and substituting the earlier derived result $\tilde{M} = M_0 e^{jkz_0}$ into (20) and (21). In matrix notation, the resulting equations are

$$\begin{bmatrix} F_x \\ F_z \end{bmatrix} = \eta_0 M_0 G e^{-kx_0} \begin{bmatrix} -sin(kz_0) & cos(kz_0) \\ cos(kz_0) & sin(kz_0) \end{bmatrix} \begin{bmatrix} I_1 \\ I_2 \end{bmatrix} \tag{22}$$

where several constants have been collected into $G = \frac{A_m \mu_0}{4k}(1 - e^{-k\Delta})$. The x_0 and z_0 dependencies are explicitly retained since these variables represent motion of the magnet array relative to the stator. This completes the derivation of the motor force equations.

3 Commutation and control

In operation, the motor will be used under closed-loop control. A loop controlling two degrees of freedom with a single linear motor is shown in block diagram form in Figure 8. Here we assume that a single linear motor is attached to a mass M which is allowed to move in only two degrees of freedom x and z. This is the same as assuming that the motor drives through the center of mass. If this assumption is not met, then the model will be more densely interconnected, but the control issues remain essentially unchanged. The linear motor currents I_1 and I_2 are assumed to be driven by a current amplifier. The current setpoints I_{s1} and I_{s2} are generated by the block labelled Commutation Laws. The function of this block is to determine these setpoints such that the motor applies forces F_x and F_z which are equal to the desired forces F_{dx} and F_{dz}. If this is properly accomplished, then the system appears linear and decoupled from inputs F_{dx} and F_{dz} to outputs x and z, and can be controlled by two independent linear compensators which act on errors e_x and e_z.

The commutation laws which achieve this decoupling are derived by inverting (22) to yield

$$\begin{bmatrix} I_{s1} \\ I_{s2} \end{bmatrix} = \frac{e^{kx_0}}{\eta_0 M_0 G} \begin{bmatrix} -sin(kz_0) & cos(kz_0) \\ cos(kz_0) & sin(kz_0) \end{bmatrix} \begin{bmatrix} F_x \\ F_z \end{bmatrix}. \tag{23}$$

This system of equations takes the desired normal and tangential forces and maps them to the currents needed to produce these forces. To the extent that the commutation laws are accurate, this decouples the two degrees of freedom.

4 Power dissipation

In a specific implementation, the maximum available force is limited by power dissipation in the stator windings. To develop the thermal limits imposed on the motor design, the power dissipation for a single sinusoidally distributed phase is calculated as follows. The power density in a region of conductivity σ carrying current density J is

$$P = \frac{J^2}{\sigma}. \tag{24}$$

In general, the current density is

$$J = \mathrm{Re}\tilde{J}e^{-jkz} = \mathrm{Re}(\tilde{J})\cos(kz) + \mathrm{Im}(\tilde{J})\sin(kz). \tag{25}$$

With only a single phase excited, J becomes

$$J = I_1\eta_0\cos(kz). \tag{26}$$

The differential power element is

$$dP = \frac{I_1^2\eta_0^2 w\Delta}{\sigma}\cos^2(kz)dz \tag{27}$$

The power dissipation P_λ per spatial wavelength $\lambda = \frac{2\pi}{k}$ is determined by integrating equation (27) over this wavelength. Thus

$$P_\lambda = \int_0^{\frac{2\pi}{k}} \frac{I_1^2\eta_0^2 w\Delta}{\sigma}\cos^2(kz)dz. \tag{28}$$

Evaluating this integral gives

$$P_\lambda = \frac{I_1^2\eta_0^2 w\Delta\lambda}{2\sigma}. \tag{29}$$

A prototype linear motor stator of length $l = 50.8 \times 10^{-3}$, width $w = 0.102$m, depth $\Delta = 7.62 \times 10^{-3}$m, spatial wavelength $\lambda = 50.8 \times 10^{-3}$m, and winding density $\eta_0 = 4.4 \times 10^6$turns/m^2 was constructed using number 26 copper wire. When supplied with approximately 10 W, this stator experiences a temperature rise of 50°C. This experiment provides an estimate of 5°C/W for the stator temperature coefficient in this geometry .

For a two-phase motor of these dimensions, with a phase current $I_1 = 1$A, equation (22) yields a force level of 33.8 N. This force is sufficient to accelerate a 10 kg platen at more than 0.3 times the acceleration of gravity. At this current, equation (29) yields a power dissipation of 6.8 W. Using the temperature coefficient developed above, this results in a temperature rise of 34°C.

This temperature rise is well within the thermal limits of the motor materials, but is still a large power dissipation in the context of a precision machine, as the resulting thermal expansion can destroy machine accuracy. This problem can be addressed by taking advantage of the force/power scaling laws. Specifically, since power increases as the square of current, and force increases linearly with current, if the motor area is increased by a factor of n, then the current required to achieve a given force is reduced by this factor. However, with this reduced current, the power density is reduced by n^2, and thus the total power is reduced by n. Thus it is likely that a larger motor will be used in the final design.

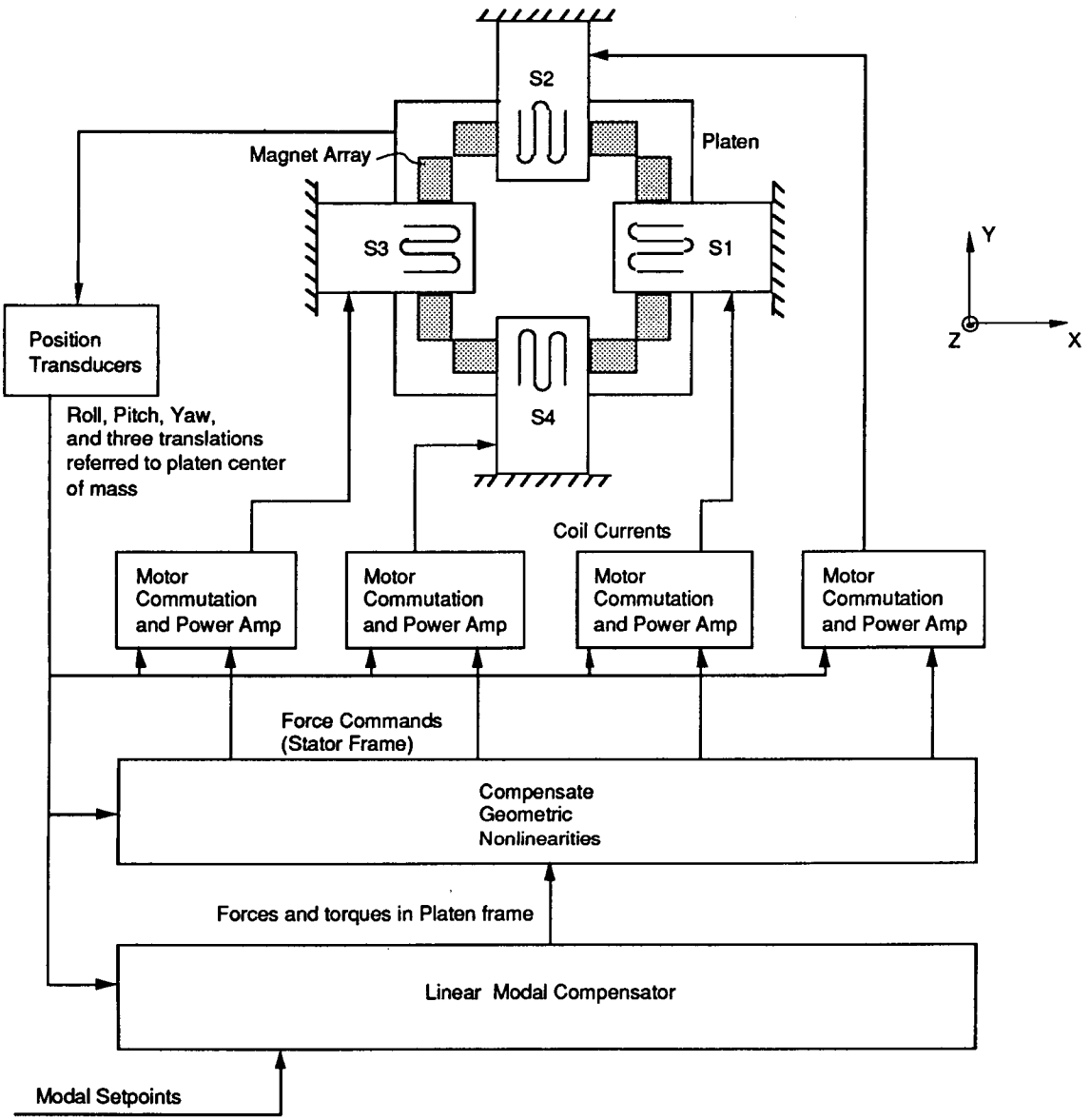

Figure 9: X-Y stage block diagram.

5 Magnetic bearing X-Y stage

Given a magnetic suspension linear motor as developed above, various stage geometries are possible. One such geometry is shown in Figure 9. Here, four linear suspension motors are combined to act on the top surface of a platen to implement an X–Y stage suitable for photolithography. The stators are labelled $S1$ through $S4$ and drive against four magnet arrays which are shown as grey rectangles. Stators $S1$ and $S3$ drive the platen in the Y-direction and stators $S2$ and $S4$ drive the platen in the X-direction. The four stators are driven appropriately to control the remaining four platen degrees of freedom.

The Linear Modal Compensator block consists of separate lead/lag compensators for each of the six degrees of freedom. The Compensate Geometric Nonlinearities block inverts the kinematic relations to translate forces and torques specified in the platen frame (where the system appears as linear) into forces specified in the stator frame (where they are actually applied to the platen). The Motor Commutation and Power Amp blocks each implement (23) for their respective stator assembly and contain power amplifiers for each of the stator phases.

This X-Y stage represents the long-term focus of our design efforts. In order to gain experience with the construction and control of the linear motor, the linear bearing system of Figs. 2–4 will be used as a test-bed for a single linear suspension motor. The design will be refined here before advancing to the X-Y system shown in Fig. 6.

6 Conclusions and suggestions for further work

We have shown the design and analyzed the electromechanics of a linear motor suitable for independently controlling two suspension degrees of freedom. This motor, at least on paper, meets the requirements for driving an X-Y stage of 10 kg mass with about 4 m/sec^2 acceleration, with travel of several hundred millimeters in X and Y, and with reasonable power dissipation. A conceptual design for such a stage has been presented.

However, this design has not yet been verified experimentally. A prototype of the linear motor is in construction and will be tested shortly. Initial testing is expected to take the form of operating the linear motor on a multi-axis load-cell in order to determine the extent to which the actual motor operation matches the theory developed herein. The commutation laws can then be modified based upon experimental data. Once the motor operation is verified experimentally, a single linear motor will be attached to the linear bearing as shown in Figures 2–4, in order to gain experience with control issues. After satisfactory testing on the linear bearing, the system shown in Figure 9 will be constructed in order to achieve the end goal of control of planar motion with 200 mm travel.

The systems described above can be improved in several ways. Currently, the linear bearing operates with purely linear control of the seven support electromagnets. The large-signal closed-loop performance of the bearing could be improved by including nonlinear compensation of the electromagnet force characteristic, as described in [6]. Additionally, the background noise of the five capacitive sensors currently limits the position stability. Thus it would be fruitful to investigate improved sensor techniques. Also, further work is needed in

developing sufficiently accurate and robust control techniques for the multivariable bearing system. Here, mechanical and electrical noise sources, uncertainties in the plant parameters, quantization of signals in the discrete-time controllers, saturation of power amplifiers and other non-idealities need to be considered as they impact the overall system performance. Finally, the magnet array technology developed by Halbach for linear accelerators [7,8] appears to be highly applicable to the linear motor magnet array. These magnet arrays use rotated blocks of magnets to provide a highly sinusoidal magnetic field concentrated on only a single side of the magnet array and thus a stronger fundamental component to interact with the stator winding. A magnet array using Halbach's topology is currently in design.

In conclusion, this paper has demonstrated the theoretical feasibility of linear and planar bearings using single or multiple magnetic suspension linear motors. It remains to demonstrate this feasibility experimentally, and we are proceeding in this direction.

References

[1] Slocum, A.H., and Eisenhaure, D.B., "Design Considerations for Ultra-Precision Magnetic Bearing Supported Slides," NASA Magnetic Suspension Technology Conference, Hampton, Va. Feb. 2–4, 1988.

[2] Trumper, D.L., "Magnetic Suspension Techniques for Precision Motion Control," Ph.D. Thesis, Dept. of Elec. Eng. and Comp. Sci., M.I.T., Camb., Mass., Sept., 1990.

[3] Teague, E.C., "The National Institute of Standards and Technology molecular measuring machine project: Metrology and precision engineering design," *Journal of Vacuum Science Technology*, B7 (6), Nov/Dec, 1989, pp. 1898-1902.

[4] Trumper, D.L., and Slocum, A. H., "Five-Degree-of-Freedom Control of an Ultra-Precision Magnetically-Suspended Linear Bearing," NASA Workshop on Aerospace Applications of Magnetic Suspension Technology, NASA Langley Research Center, Hampton, VA, Sept. 25–27, 1990.

[5] Melcher, J.R., *Continuum Electromechanics* , MIT Press, Camb., Mass., 1981.

[6] Trumper, D.L., "Nonlinear Compensation Techniques for Magnetic Suspension Systems," NASA Workshop on Aerospace Applications of Magnetic Suspension Technology, Hampton, VA, Sept. 25–27, 1990.

[7] Halbach, K., "Design of Permanent Multipole Magnets with Oriented Rare Earth Cobalt Material," Nuclear Instruments and Methods, 169, 1980, pp. 1–10, North-Holland Publishing Co.

[8] Halbach, K., "Physical and Optical Properties of Rare Earth Cobalt Magnets," Nuclear Instruments and Methods, 187, 1981, pp. 109–117, North-Holland Publishing Co.